

1

2 **Supplementary Information for**

3 **Mechanistic framework for reduced-order models in soft materials: Application to** 4 **three-dimensional granular intrusion**

5 **Shashank Agarwal, Daniel I Goldman, Ken Kamrin**

6 **Ken Kamrin**

7 **E-mail: kkamrin@mit.edu**

8 **This PDF file includes:**

- 9 Supplementary text
- 10 Figs. S1 to S8
- 11 Tables S1 to S4
- 12 SI References

13 **Supporting Information Text**

14 **S1. Pre-existing 3D-RFT forms**

The form of 3D-RFT proposed by Treers et al. (1) has the following formulation:

$$\mathbf{F} = \int_S [f_1(\tilde{\psi}, \tilde{\gamma}) \alpha_y(\tilde{\gamma}, \tilde{\beta}) \hat{\mathbf{e}}_1 + f_{23}(\tilde{\psi}, \tilde{\gamma}) (-\alpha_x(\tilde{\gamma}, \tilde{\beta}) \hat{\mathbf{e}}_2 + \alpha_z(\tilde{\gamma}, \tilde{\beta}) \hat{\mathbf{e}}_3)] |z| dA \quad [1]$$

where the direction $\hat{\mathbf{e}}_2$ represents the direction of the horizontal component of surface normal $\hat{\mathbf{n}}$, $\hat{\mathbf{e}}_3$ represents the vertical direction, and $\hat{\mathbf{e}}_1$ represents the cross product of $\hat{\mathbf{e}}_2$ and $\hat{\mathbf{e}}_3$. The angles $\tilde{\beta}$, $\tilde{\psi}$, and $\tilde{\gamma}$ characterize the plate and velocity directions in terms of basis directions $\hat{\mathbf{e}}_1$, $\hat{\mathbf{e}}_2$, and $\hat{\mathbf{e}}_3$. We use a ‘~’ with these angles to differentiate them from the characteristic angles β , γ , and ψ we use in the current work. Altogether,

$$\begin{aligned} \hat{\mathbf{e}}_3 &= \hat{\mathbf{z}} & \hat{\mathbf{e}}_2 &= \frac{\hat{\mathbf{n}} - (\hat{\mathbf{n}} \cdot \hat{\mathbf{z}}) \hat{\mathbf{z}}}{|\hat{\mathbf{n}} - (\hat{\mathbf{n}} \cdot \hat{\mathbf{z}}) \hat{\mathbf{z}}|} = \frac{(n_x, n_y, 0)}{\sqrt{n_x^2 + n_y^2}} & \hat{\mathbf{e}}_1 &= \hat{\mathbf{e}}_2 \times \hat{\mathbf{e}}_3 \\ \tilde{\gamma} &= \tan^{-1} \left(-\frac{\mathbf{v} \cdot \hat{\mathbf{e}}_3}{\mathbf{v} \cdot \hat{\mathbf{e}}_2} \right) = \tan^{-1} \left(-\frac{v_z \sqrt{n_x^2 + n_y^2}}{v_x n_x + v_y n_y} \right) & \tilde{\psi} &= \tan^{-1} \left(\frac{\mathbf{v} \cdot \hat{\mathbf{e}}_2}{\mathbf{v} \cdot \hat{\mathbf{e}}_1} \right) = \tan^{-1} \left(\frac{v_x n_x + v_y n_y}{v_x n_y - v_y n_x} \right) \\ \tilde{\beta} &= \tan^{-1} \left(\frac{n_z}{\sqrt{n_x^2 + n_y^2}} \right) - \frac{\pi}{2} \times \text{sign}(\hat{\mathbf{n}} \cdot \hat{\mathbf{z}}). \end{aligned}$$

15
16 The form was also used by Huang et al. (2) with a few minor modifications to the choices of the fittings functions f_1 and f_{23} .
17 We present two example cases of the limitations of this form, which show that in some situations it is too restrictive, while in
18 others it is not restrictive enough.

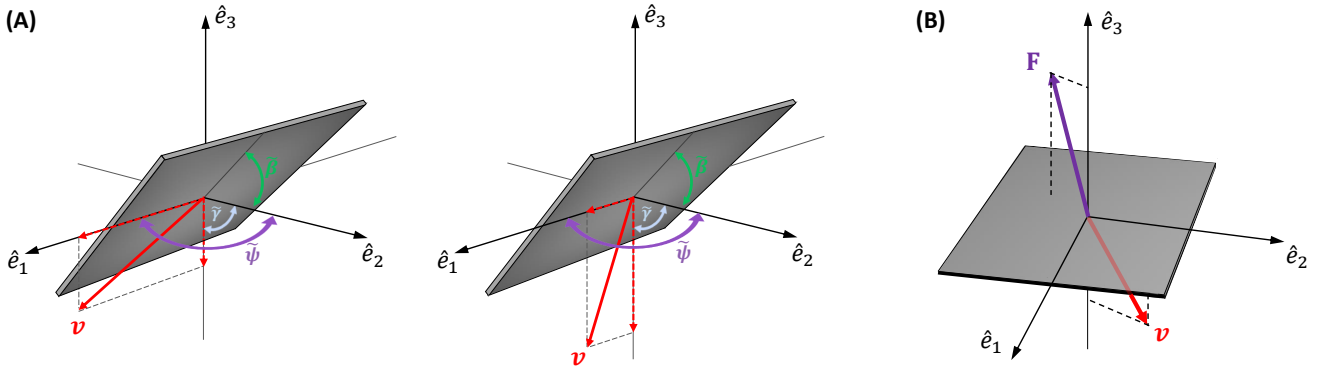


Fig. S1. Pre-existing 3D-RFT verification: (A) Case 1 — An example of an inappropriate system representation in pre-existing 3D-RFT. The two cases represent two different plate motions (same plate orientations but different velocity directions (\mathbf{v}) in $\hat{\mathbf{e}}_1 \hat{\mathbf{e}}_3$ plane), yet the form assigns identical characteristic angles ($\tilde{\beta}, \tilde{\gamma} = \pi/2, \tilde{\psi} = \pi/2$) to define them. Thus, the 3D-RFT form predicts identical forces even though the two motions are expected to experience different resistive forces. (B) Case 2 — A plate oriented at $\tilde{\beta} \rightarrow 0$. The global symmetry constraint requires the force (\mathbf{F}), the velocity (\mathbf{v}), and the gravity (\mathbf{g}) to be co-planar i.e. \mathbf{F} should lie in \mathbf{vz} plane as shown in the figure as $\tilde{\beta} \rightarrow 0$. The pre-existing 3DRFT form does not satisfies this requirement.

19 In the first case, we consider a surface element oriented with a normal vector direction $\hat{\mathbf{n}}$ and moving at a velocity \mathbf{v} such
20 that $\mathbf{v} \cdot \hat{\mathbf{e}}_2 = 0$, i.e. $v_x n_x + v_y n_y = 0$. This corresponds to a velocity vector lying in the vertical plane that contains the
21 horizontal tangent line of the plate. Based on the definitions above, this form of 3D-RFT requires the resistive force vector in
22 this case to be independent of $|v_z|$. For example, a surface moving in any direction in the positive quadrant of the $\hat{\mathbf{e}}_1 \hat{\mathbf{e}}_3$ plane is
23 assumed to experience the same resistive force vector, since these motions always produce the same angles and same $\hat{\mathbf{e}}$'s. But
24 this force response is not what is observed, nor what one would expect; using the angles defined in the main text, it corresponds
25 to the proposition that the force does not change when varying γ at constant β and $\psi = \pi/2$ but the reference data in Figure
26 S8 show that in fact the force varies rather strongly with γ . Hence, this form of 3D-RFT in this case **over-constrains** the
27 force response.

In the second case, we consider the IRT sub-constraint shown in Figure 3C of the main text which requires that in the limit of tilt approaching zero ($\tilde{\beta} \rightarrow 0$), the force should lie in the \mathbf{vz} -plane i.e. $\lim_{\tilde{\beta} \rightarrow 0} (\mathbf{F} \cdot (\hat{\mathbf{v}} \times \hat{\mathbf{e}}_3)) = 0$ for all $\tilde{\psi}$ and $\tilde{\gamma}$. Upon

substituting the above forms, we get:

$$\begin{aligned}
\mathbf{F} \cdot (\mathbf{v} \times \hat{\mathbf{e}}_3) &= \hat{\mathbf{e}}_3 \cdot (\mathbf{F} \times \mathbf{v}) = F_1 v_2 - F_2 v_1 \\
&= f_1(\tilde{\psi}, \tilde{\gamma}) \alpha_y(\tilde{\gamma}, \tilde{\beta}) |\mathbf{v} - (\mathbf{v} \cdot \hat{\mathbf{z}})\hat{\mathbf{z}}| \cos \tilde{\psi} + f_{23}(\tilde{\psi}, \tilde{\gamma}) \alpha_x(\tilde{\gamma}, \tilde{\beta}) |\mathbf{v} - (\mathbf{v} \cdot \hat{\mathbf{z}})\hat{\mathbf{z}}| \sin \tilde{\psi} \\
&= (f_1(\tilde{\psi}, \tilde{\gamma}) \alpha_y(\tilde{\gamma}, \tilde{\beta}) \cos \tilde{\psi} + f_{23}(\tilde{\psi}, \tilde{\gamma}) \alpha_x(\tilde{\gamma}, \tilde{\beta}) \sin \tilde{\psi}) \times |\mathbf{v} - (\mathbf{v} \cdot \hat{\mathbf{z}})\hat{\mathbf{z}}| \\
&= (-f_1(\tilde{\psi}, \tilde{\gamma}) \alpha_x(0, 0) \cos \tilde{\psi} + f_{23}(\tilde{\psi}, \tilde{\gamma}) \alpha_x(\tilde{\gamma}, \tilde{\beta}) \sin \tilde{\psi}) \times |\mathbf{v} - (\mathbf{v} \cdot \hat{\mathbf{z}})\hat{\mathbf{z}}| \quad [\text{Using } \alpha_y \text{ definiton from Treers et al. (1)}] \\
&= (-f_1(\tilde{\psi}) \alpha_x(0, 0) \cos \tilde{\psi} + f_{23}(\tilde{\psi}) \alpha_x(\tilde{\gamma}, \tilde{\beta}) \sin \tilde{\psi}) \times |\mathbf{v} - (\mathbf{v} \cdot \hat{\mathbf{z}})\hat{\mathbf{z}}|.
\end{aligned}$$

28 Note that we drop the $\tilde{\gamma}$ dependence of f_1 and f_{23} in the final step using the definitions from Treers et al. (1). Utilizing the
29 fact that $|\mathbf{v} - (\mathbf{v} \cdot \hat{\mathbf{z}})\hat{\mathbf{z}}| = |\mathbf{v}|(1 + \tan^2 \tilde{\gamma} \cos^2 \tilde{\psi})^{-1/2}$ we obtain

$$\lim_{\tilde{\beta} \rightarrow 0} (\mathbf{F} \cdot (\hat{\mathbf{v}} \times \mathbf{e}_3)) = (-f_1(\tilde{\psi}) \alpha_x(0, 0) \cos \tilde{\psi} + f_{23}(\tilde{\psi}) \alpha_x(\tilde{\gamma}, 0) \sin \tilde{\psi}) (1 + \tan^2 \tilde{\gamma} \cos^2 \tilde{\psi})^{-1/2}$$

31 which is a non-trivial function of the two angles; it is not the zero function as it must be. The only way the expression
32 above vanishes identically is if $\alpha_x(\tilde{\gamma}, 0) = C$ and $f_1(\tilde{\psi}) = C f_{23}(\tilde{\psi}) \tan \tilde{\psi} / \alpha_x(0, 0)$ for some constant C , which would be a very
33 heavy-handed fit that would certainly not fit a range of data (and was not close to how those functions were fit in Treers et al.
34 (1)). Thus, in this case, the chosen form **under-constrains** the force response and misses out on an important constraint the
35 surface force response should follow.

37 S2. Application of the 3-step procedure to other material models of soft media

38 The main text focuses on applying the general three-step procedure to deduce three-dimensional RFT for granular media. It
39 is instructive to see how the methodology would be applied in other cases. This is primarily so for Steps 1 and 2, since the
40 rotation symmetry of Step 3 is universal across all isotropic materials.

41 First of all, it bares noting that the quality of the approximation one obtains from a reduced-order intrusion model varies
42 as one varies the underlying continuum model. In (3), a pseudo-diagnostic test was devised to assess the level of accuracy
43 one might expect from the localization hypothesis (presumed in Step 1) as one varies the underlying rheological model. This
44 so-called ‘‘garden hoe test’’ considers whether a localized rule for the surface stress,

$$\mathbf{F}^{\text{total}} = \int_{\text{surf}} \mathbf{t}(\hat{\mathbf{n}}, \mathbf{v}, \mathbf{g}, |z|; \text{mat}) ds \quad [2]$$

46 could possibly agree with full continuum-level solutions of the intrusion force. This test assesses the question by considering a
47 very simple family of intruders — finite-sized square plates moving in arbitrary directions at arbitrary tilts. What varies as one
48 changes the rheological model is the parameter set invoked by *mat*. In frictional media, as in the main text, $\text{mat} = \{\rho_c, \mu_s, \mu_w\}$;
49 in purely cohesive solids $\text{mat} = \{\rho, \sigma_y\}$ for yield stress σ_y ; in viscous fluids $\text{mat} = \{\rho, \eta\}$ for viscosity η ; in inviscid (Euler)
50 fluids $\text{mat} = \{\rho\}$; and so on. For each *mat*, dimensional analysis and physical constraints of the continuum PDE’s put strong
51 restrictions on how the surface traction formula $\mathbf{t}(\cdot)$ is allowed to depend on its inputs. To deduce if a material ‘‘passes’’ the
52 garden hoe test, one uses this constrained form for the $\mathbf{t}(\cdot)$ function to infer the resistive force on a finite-sized square intruding
53 plate and then compares this answer to a known full-field result from the continuum theory. Some material models pass the
54 garden hoe test — the localized force formula agrees exactly with the result one would obtain from the full continuum solution
55 — while others do not. For example, frictional media, purely cohesive solids, and inviscid fluids pass the test, but viscous fluids
56 do not. Interestingly, we have observed that materials which pass the garden hoe test also happen to display a strong collapse
57 to the RFT approximation in general, that is, when non-rectangular intruders are used (3). We do not have a complete proof
58 for this.

59 In contrast to cohesionless grains, gravity and intruder depth play a smaller role in intrusion problems in media with
60 pressure-insensitive shear stress (aside from a standard bouyancy term). We show three examples next in this limit, where
61 possible dependence on $|z|$ and \mathbf{g} is neglected.

For cohesive materials with a constant rate-independent yield stress, such as muds or foams in a certain slow limit, the
corresponding RFT-like rule after Steps 1 and 2 is

$$\text{Cohesive media:} \quad \mathbf{t} = \sigma_y \mathbf{a}^{\text{gen}}(\hat{\mathbf{n}}, \hat{\mathbf{v}})$$

62 for some dimensionless universal function $\mathbf{a}^{\text{gen}}(\cdot)$. The form for the traction shown above is the only dimensionally sound
63 formula for the given material property set in the slow limit. And when the above relation is tested in non-flat-plate intrusion
64 tests and compared to full-field results, a high-level agreement is observed (3) indicative of strong general accuracy of the
65 reduced-order RFT formula.

Unlike the previous examples, which are considered in the inertialess limit, for inviscid fluids the intrusion force arises solely
from the inertia transferred to the fluid. Hence, in this case, after Step 2, one has the following dimensionally-sound local
traction form

$$\text{Inviscid fluid:} \quad \mathbf{t} = \rho v^2 \mathbf{b}^{\text{gen}}(\hat{\mathbf{n}}, \hat{\mathbf{v}})$$

66 for some dimensionless universal function $\mathbf{b}^{\text{gen}}(\cdot)$. The resulting form produces an accurate model for locomotion of swimming
 67 centipedes (4) and has been indirectly validated through the success of the so-called ‘‘Blade Element Theory’’ of rotor design
 68 (5), which uses a similar localization rule to determine drag and lift forces for generically shaped rotors moving through an
 69 inviscid fluid.

In materials that do not pass the garden hoe test, we can still obtain a best possible approximate reduced-order model
 for intrusion, even if its accuracy may never rise to the level seen in frictional or cohesive media. In these cases, additional
 information can be used to obtain an approximate localization rule. A useful case in point is viscous media, which does not
 pass the garden hoe test because the force on an intruding square plate of size L in a large domain of viscous media must have
 the form

$$\mathbf{F}^{\text{total}} = L\eta v \mathbf{c}^{\text{gen}}(\hat{\mathbf{n}}, \hat{\mathbf{v}})$$

70 for some dimensionless function $\mathbf{c}^{\text{gen}}(\cdot)$. The linearity in v is required due to linearity in the Stokes equations. Since the force
 71 does not scale as L^2 a localized superposition rule of the form of Eq. (2) will not be precise even for simple plate intruders.
 72 However, and as is the tradition for viscous RFT going back to Gray and Hancock (6), one can assert an additional length-scale
 73 λ within the force model to obtain an approximate form. One can use the entire diameter of the immersed object as λ , or, in
 74 the case of viscous quasi-1D swimmers, one often uses the wavelength of the swimming mode. However it is chosen, we can
 75 then write the quasi-local form for the mean traction on a plate of size λ in viscous fluid as

$$\text{Viscous fluid:} \quad \mathbf{t} = \frac{\eta v}{\lambda} \mathbf{c}^{\text{gen}}(\hat{\mathbf{n}}, \hat{\mathbf{v}})$$

76 Utilizing this relation in Eq. (2) gives a result that only matches the exact solution for a finite plate in the case that the plate
 77 has a size of $L = \lambda$. However, even when this is not the case, the formula can still be used as an approximation.

78 S3. Verification of leading edge hypothesis in 3D-RFT

79 We verify the applicability of the ‘leading-edge hypothesis’ (ie., the assumption that no force occurs on surfaces with $\mathbf{n} \cdot \mathbf{v} \leq 0$)
 80 during three-dimensional plate motion. To verify the hypothesis, we plot the variations of forces on the front and the back
 81 surface-nodes of the plate geometry used for generating the reference 3D-RFT graphs. Figure S2 shows the variations of
 82 force magnitudes on the two surfaces the plates used for modeling intrusions. We plot these results for six plate and velocity
 83 configurations. The sides are color-coded in blue and red. In the first two cases, the front-face (in red) acts as the leading edge.
 84 In the next two cases, the back-face (in blue) acts as the leading edge. In all such cases, we measure leading edges forces, as
 85 non-leading edge forces are negligible in comparison to leading-edge forces. In the last two cases, both the faces experience
 86 equal force magnitudes with (equal tangential forces but equal and opposite normal forces). The last two cases correspond to
 87 the slicing motion of the surfaces. We take average force magnitudes for making RFT plots in such cases. We observed similar
 behavior in other plate and velocity configurations.

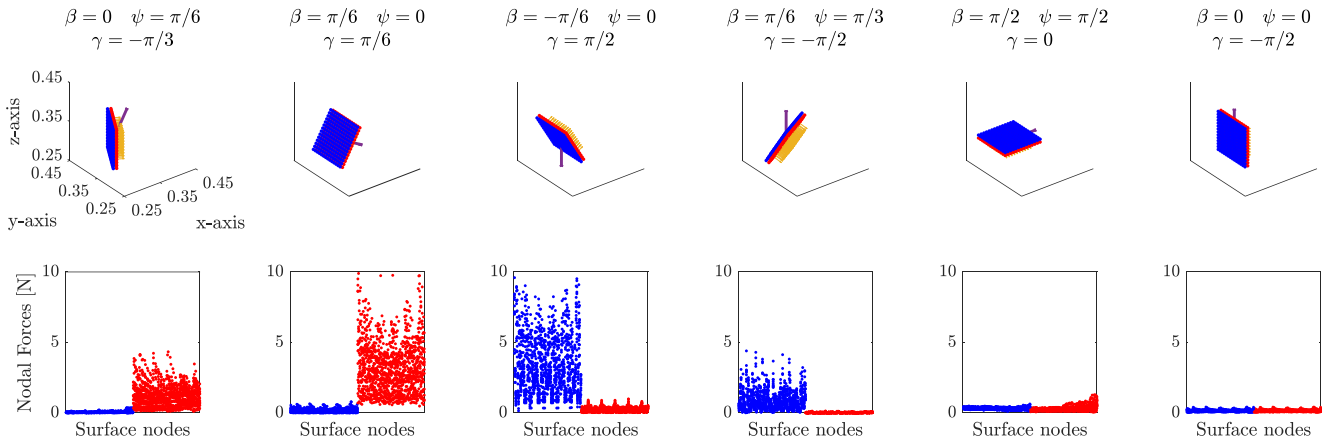


Fig. S2. Leading edge hypothesis verification: Variation of the magnitude of forces on the two sides of thin plates during granular intrusions. The sides are color-coded in blue and red. The yellow arrows show front-face normals, and the violet arrow shows the velocity direction. We plot six combinations of plate configurations and velocity directions. In the first two cases, the front-face (in red) acts as the leading edge. In the next two cases, the back-face (in blue) acts as the leading edge. And in the last two cases, both the faces experience equal force magnitudes with (equal tangential forces but equal and opposite normal forces). The last two cases correspond to the slicing motion of the surfaces. We take average force magnitudes for making RFT plots in such cases.

88

89 S4. Reference data generation; internal friction (μ_{int}) dependence of 3D-RFT

90 We use a large combination of material properties ($\rho_c, \mu_{\text{int}}, \mu_{\text{surf}}$) and 3D-RFT reference variables (β, γ, ψ) to generate continuum
 91 modeling-based reference data for evaluating the 3D-RFT form. In regards to the material properties we use five material

92 internal friction values ($\mu_{\text{int}} = [0.3, 0.4, 0.5, 0.7, 0.9]$) with two values of surface friction (μ_{surf}) in each case. For $\mu_{\text{int}} = 0.4$ we
 93 use 3 instead of 2 μ_{surf} values. For each of the 11 combinations of μ_{int} and μ_{surf} , we conduct plate intrusions at 7 combinations
 94 of plate tilt angle ($\beta = -\pi/2 : \pi/6 : \pi/2$ rad), 7 combinations of velocity direction angle ($\gamma = -\pi/2 : \pi/6 : \pi/2$ rad), and 4
 95 combinations of plate twist angle ($\psi = 0 : \pi/6 : \pi/2$ rad). For the $\{\mu_{\text{int}} = 0.40, \mu_{\text{surf}} = 0.15\}$, we use 13 combinations of β
 96 ($\pi/2 : \pi/6 : \pi/2$ rad), 13 combinations of γ ($-\pi/2 : \pi/6 : \pi/2$ rad), and 4 combinations of ψ ($0 : \pi/6 : \pi/2$ rad). Additionally,
 97 we conduct plate intrusion simulations at $\{\mu_{\text{int}} = 0.2, \mu_{\text{surf}} = 0.2\}$ and $\{\mu_{\text{int}} = 0.1, \mu_{\text{surf}} = 0.1\}$ at $\psi = 0$ rad to evaluate ξ_n at
 98 $\mu_{\text{int}} = 0.1$ and 0.2 . We do not explore ψ in $[-\pi/2 : 0]$ rad range for the reference data as α_r , α_z , and α_θ are known to be even,
 99 even, and odd (resp.) in ψ from ‘plate twist symmetry’. The polynomial fits for f_1 , f_2 , and f_3 are provided in Tables S3 and S4.

100 We explore the dependence of 3D-RFT forces on material internal friction by conducting plate intrusion simulations for
 101 five different values of (μ_{int}) at two values of surface friction (μ_{surf}) each (except $\mu_{\text{int}} = 0.4$ for which we explore 3 values of
 102 μ_{surf}). To better understand the trends in variations of α , we only consider the normal component of α i.e. α_n . Figure S3
 103 shows values of α_n scaled by the scaling coefficient ξ_n . These plots show that ξ_n primarily depends on μ_{int} (in addition to its
 104 linear dependence of ρ_c and g , i.e. $\xi_n = \rho_c g \hat{f}(\mu_{\text{int}})$). Figure S4 shows the variation of $\xi_n / \rho_c g$ with μ_{int} . This figure uses two
 105 additional values of μ_{int} — 0.1 and 0.2. We conducted additional simulations at limited μ_{surf} and ψ for these μ_{int} 's for better
 106 understandings the ξ_n vs μ_{int} trends, as discussed in Materials and Methods section. We find superlinear dependence of ξ_n on
 107 μ_{int} , which was also observed by researchers (7). Figure S4 can be used for interpreting the value of ξ_n from ρ_c , g , and μ_{int} (or
 108 the angle of repose, $\theta = \tan^{-1}(\mu_{\text{int}})$) of a non-cohesive granular media. Exact values of ξ_n and μ_{int} corresponding to Figure S4
 109 are given in Table S1.

110

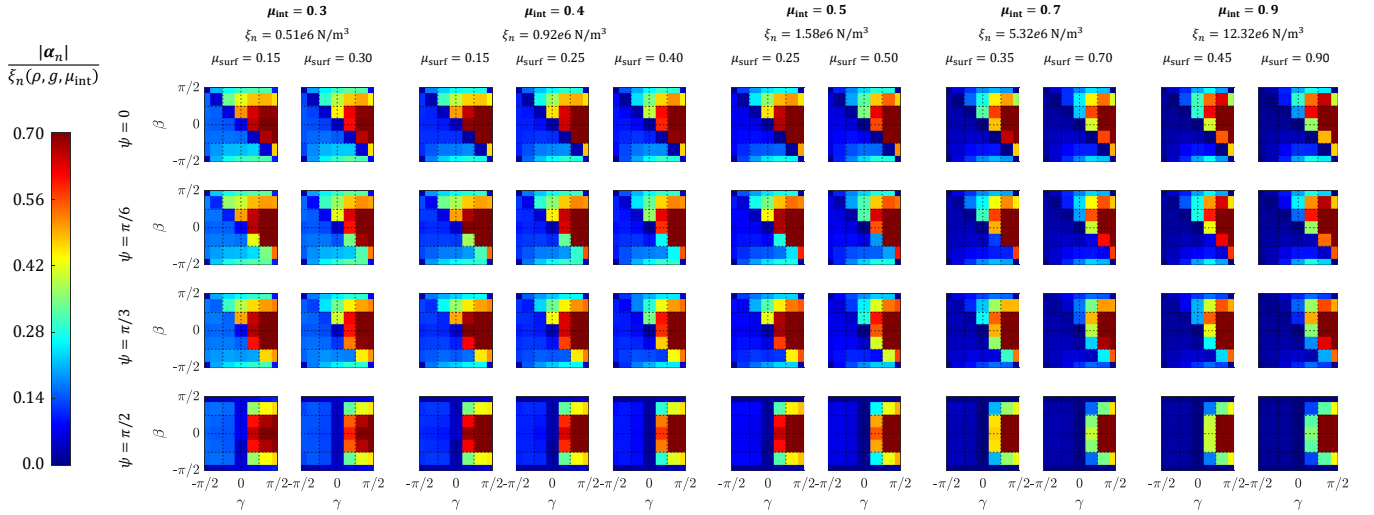


Fig. S3. Variation of α_n with μ_{int} : Variation of normal component of stress/depth (scaled by ξ_n) for various combinations of μ_{int} and μ_{surf} . The variations of normalized ξ_n with μ_{int} are plotted in figure S4. Corresponding values of μ_{int} , μ_{surf} , and ξ_n are written at the top of each column. The granular material had an effective density of (ρ_c) 3000 kg/m³ in the cases.

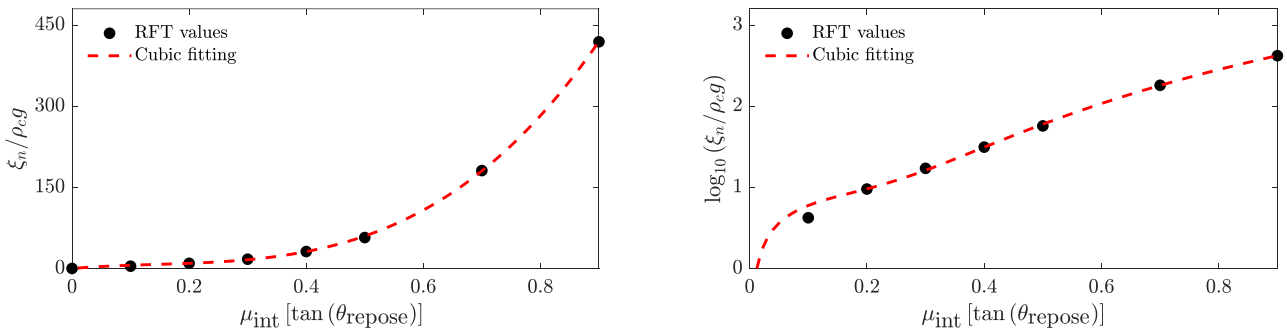


Fig. S4. Variation of ξ_n with material properties: Variation of normalized scaling coefficient ξ_n (normalized with density ρ_c and gravity g) with material internal coefficient of friction (μ_{int}) on (A) linear and (B) logarithmic scale. The cubic fitting (red dotted lines) is $\xi_n^{\text{fit}} = \rho_c g (894\mu_{\text{int}}^3 - 386\mu_{\text{int}}^2 + 89\mu_{\text{int}})$. Corresponding values are given in table S1.

Table S1. Variation of ξ_n with μ_{int} at $\rho_c = 3000 \text{ kg/m}^3$

μ_{int}	$\theta_{\text{repose}} [^\circ]$	$\xi_n [\times 10^6 \text{ N/m}^3]$
0.0	0°	0.0
0.1	5.7°	0.13
0.2	11.3°	0.28
0.3	16.7°	0.51
0.4	21.8°	0.92
0.5	26.5°	1.58
0.7	35.0°	5.32
0.9	42.0°	12.32

111 **S5. Surface friction (μ_{surf}) dependence of 3D-RFT**

112 Similar to μ_{int} , we explore the dependence of 3D-RFT forces on material-body surface friction (μ_{surf}) by conducting plate
 113 intrusions at different combinations of μ_{int} and μ_{surf} . To better understand the trends, we consider the ratio of the normal and
 114 tangential components of α i.e. $|\alpha_t|/|\alpha_n|$. Figure S5 shows values of α_n scaled by the scaling coefficient ξ_n discussed in the
 115 previous section and shown in figure S4. The plots show that the ratio $|\alpha_t|/|\alpha_n|$ largely remains independent of μ_{int} as the
 116 graphs remain largely identical for same values of μ_{surf} at different values of μ_{int} . We also see that for $\mu_{\text{surf}}^{(1)} < \mu_{\text{surf}}^{(2)}$, the graph
 117 for the lower surface friction case appears to be obtainable from the graph at the higher friction by way of a simple cut-off that
 118 ensures non-violation of the Coulomb condition based on $\mu_{\text{surf}}^{(1)}$. Equation 7 incorporates this concept into the final form of
 119 3D-RFT. The proposed generic 3D-RFT graphs in this study correspond to $\mu_{\text{surf}} = 0.9$.

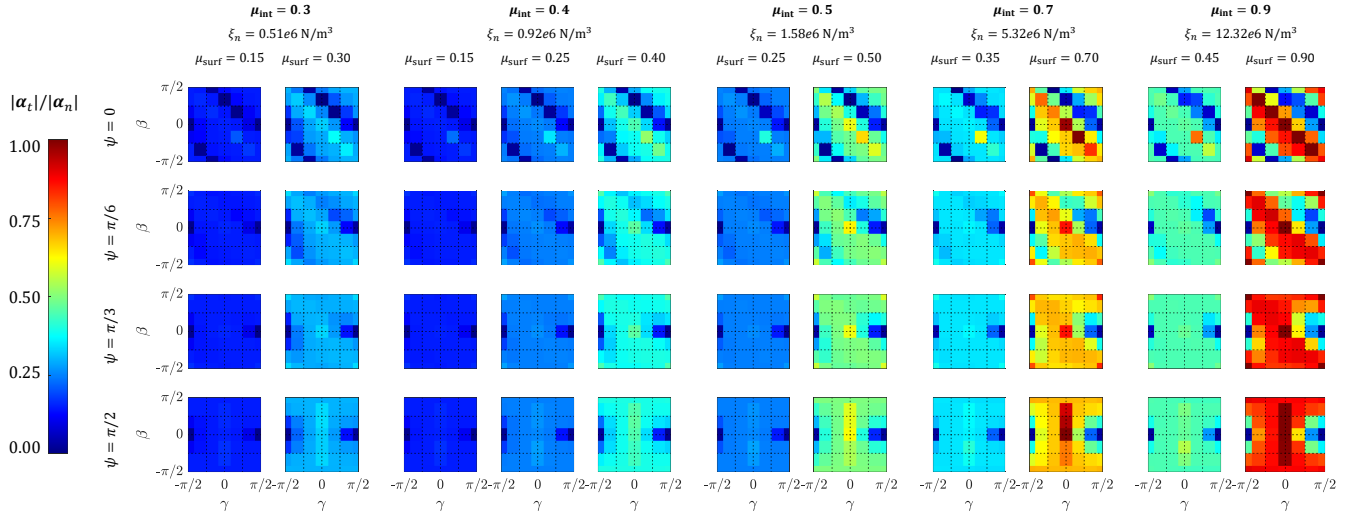


Fig. S5. Variation of $|\alpha_t|/|\alpha_n|$ with material properties: Variation of ratio of magnitude of α in tangential and normal directions. The ratio never exceeds the individual μ_{surf} values in each case due to the Coulomb friction condition. Corresponding values of μ_{int} , μ_{surf} , and ξ_n are written at the top of each column. The granular material used has an effective density of (ρ_c) 3000 kg/m^3 .

120 **S6. Proof that Coulomb friction cut-off does not affect satisfaction of global rotational symmetry constraint**

Given that α^{gen} obeys Eq 6 and thus satisfies the global rotation constraint, we want to prove that α as represented in Eq 5 for general internal and surface frictions also obeys the global rotation constraint. First, we notice that if α^{gen} obeys the rotational symmetry constraint then $\alpha_n^{\text{gen}} = \alpha^{\text{gen}} \cdot \hat{n}$ and $\alpha_t^{\text{gen}} = \alpha^{\text{gen}} - (\alpha^{\text{gen}} \cdot \hat{n}) \hat{n}$ must also obey the rotational symmetry

constraint. Under an arbitrary rotation \mathbf{R} of the inputs, Eq 5 imply

$$\begin{aligned}
& \alpha(\mathbf{R}\hat{\mathbf{n}}, \mathbf{R}\hat{\mathbf{v}}, \mathbf{R}\hat{\mathbf{g}}; \rho_c, \mu_{\text{int}}, \mu_{\text{surf}}) \\
&= \rho_c g \hat{f}(\mu_{\text{int}}) |\alpha_n^{\text{gen}}(\mathbf{R}\hat{\mathbf{n}}, \mathbf{R}\hat{\mathbf{v}}, \mathbf{R}\hat{\mathbf{g}})| \hat{\mathbf{n}} + \rho_c g \hat{f}(\mu_{\text{int}}) \min \left(\frac{\mu_{\text{surf}} |\alpha_n^{\text{gen}}(\mathbf{R}\hat{\mathbf{n}}, \mathbf{R}\hat{\mathbf{v}}, \mathbf{R}\hat{\mathbf{g}})|}{|\alpha_t^{\text{gen}}(\mathbf{R}\hat{\mathbf{n}}, \mathbf{R}\hat{\mathbf{v}}, \mathbf{R}\hat{\mathbf{g}})|}, 1 \right) \alpha_t^{\text{gen}}(\mathbf{R}\hat{\mathbf{n}}, \mathbf{R}\hat{\mathbf{v}}, \mathbf{R}\hat{\mathbf{g}}) \\
&= \rho_c g \hat{f}(\mu_{\text{int}}) |\mathbf{R}\alpha_n^{\text{gen}}(\hat{\mathbf{n}}, \hat{\mathbf{v}}, \hat{\mathbf{g}})| \mathbf{R}\hat{\mathbf{n}} + \rho_c g \hat{f}(\mu_{\text{int}}) \min \left(\frac{\mu_{\text{surf}} |\mathbf{R}\alpha_n^{\text{gen}}(\hat{\mathbf{n}}, \hat{\mathbf{v}}, \hat{\mathbf{g}})|}{|\mathbf{R}\alpha_t^{\text{gen}}(\hat{\mathbf{n}}, \hat{\mathbf{v}}, \hat{\mathbf{g}})|}, 1 \right) \mathbf{R}\alpha_t^{\text{gen}}(\hat{\mathbf{n}}, \hat{\mathbf{v}}, \hat{\mathbf{g}}) \\
&= \mathbf{R} \rho_c g \hat{f}(\mu_{\text{int}}) |\alpha_n^{\text{gen}}(\hat{\mathbf{n}}, \hat{\mathbf{v}}, \hat{\mathbf{g}})| \hat{\mathbf{n}} + \rho_c g \hat{f}(\mu_{\text{int}}) \min \left(\frac{\mu_{\text{surf}} |\alpha_n^{\text{gen}}(\hat{\mathbf{n}}, \hat{\mathbf{v}}, \hat{\mathbf{g}})|}{|\alpha_t^{\text{gen}}(\hat{\mathbf{n}}, \hat{\mathbf{v}}, \hat{\mathbf{g}})|}, 1 \right) \alpha_t^{\text{gen}}(\hat{\mathbf{n}}, \hat{\mathbf{v}}, \hat{\mathbf{g}}) \\
&= \mathbf{R}\alpha(\hat{\mathbf{n}}, \hat{\mathbf{v}}, \hat{\mathbf{g}}; \rho_c, \mu_{\text{int}}, \mu_{\text{surf}})
\end{aligned} \tag{3}$$

121 Thus, the 3D-RFT form in Eq 5 continues to satisfy IRT requirements and thus satisfy the global rotational constraint.

122 S7. 3D-RFT Implementation

We use an explicit iterative scheme to implement 3D-RFT in this study. The strategy primarily consists three parts — (1) discretizing the intruder surface into small sub-surfaces, (2) finding the sub-surface forces using sub-surface orientation angles (β and ψ), velocity angle (γ), area (ds), and depth from the free surface ($|z|$), and (3) summing over all sub-surfaces to find the net resistive force and moment response. A step-by-step implementation of the strategy is provided below:

Step 1: Discretize the intruder surface into small plane sub-surface elements. We use the open-source software, ‘Blender’ (version 2.91) for modeling and discretizing various intruder geometries in our study (using .wrl format).

Step 2: Calculate the velocity direction vector $\hat{\mathbf{v}}$, surface normal $\hat{\mathbf{n}}$, and depth from the free surface $|z|$ for each sub-surface. Repeat Steps 3-11 for each sub-surface.

Step 3: Check if $\hat{\mathbf{n}} \cdot \hat{\mathbf{v}} \geq 0$ (sub-surface is a ‘leading edge’) and $z < 0$ (sub-surface is submerged in the media). If both the conditions are met, follow Steps 4-11. If they are not, set the sub-surface resistive force to zero and consider the next sub-surface. Also, the application of 3D-RFT is limited to $|z| < O(10)L$ where L is the characteristic length of the intruder. RFT is (especially vertical force) expected to over-predict intrusion forces beyond this limit.

Step 4: Find local coordinate frame $\{\hat{\mathbf{r}}, \hat{\boldsymbol{\theta}}, \hat{\mathbf{z}}\}$ using following relations:

$$\hat{\mathbf{z}} = -\hat{\mathbf{g}} \quad \hat{\mathbf{r}} = \frac{\mathbf{v} - (\mathbf{v} \cdot \hat{\mathbf{z}})\hat{\mathbf{z}}}{|\mathbf{v} - (\mathbf{v} \cdot \hat{\mathbf{z}})\hat{\mathbf{z}}|} \quad \hat{\boldsymbol{\theta}} = \hat{\mathbf{z}} \times \hat{\mathbf{r}} \tag{4}$$

When $|\mathbf{v} - (\mathbf{v} \cdot \hat{\mathbf{z}})\hat{\mathbf{z}}|$ is zero (a sub-surface moves up or down), $\hat{\mathbf{r}}$ is set to the direction of horizontal component of the surface-normal i.e. $\hat{\mathbf{r}} = (\hat{\mathbf{n}} - (\hat{\mathbf{n}} \cdot \hat{\mathbf{z}})\hat{\mathbf{z}})/|\hat{\mathbf{n}} - (\hat{\mathbf{n}} \cdot \hat{\mathbf{z}})\hat{\mathbf{z}}|$.

Step 5: Find RFT characteristic angles $\{\beta, \gamma, \psi\}$ using $\{\hat{\mathbf{v}}, \hat{\mathbf{g}}, \hat{\mathbf{n}}\}$ and local coordinate frame $\{\hat{\mathbf{r}}, \hat{\boldsymbol{\theta}}, \hat{\mathbf{z}}\}$ as follows:

Find the surface characteristic angle β as:

$$\begin{aligned}
\beta = & \begin{aligned} & -\cos^{-1}(\hat{\mathbf{n}} \cdot \hat{\mathbf{z}}) & \text{if } \hat{\mathbf{n}} \cdot \hat{\mathbf{r}} \geq 0 \quad \& \quad \hat{\mathbf{n}} \cdot \hat{\mathbf{z}} \geq 0 \\ & +\pi - \cos^{-1}(\hat{\mathbf{n}} \cdot \hat{\mathbf{z}}) & \text{if } \hat{\mathbf{n}} \cdot \hat{\mathbf{r}} \geq 0 \quad \& \quad \hat{\mathbf{n}} \cdot \hat{\mathbf{z}} < 0 \\ & \cos^{-1}(\hat{\mathbf{n}} \cdot \hat{\mathbf{z}}) & \text{if } \hat{\mathbf{n}} \cdot \hat{\mathbf{r}} < 0 \quad \& \quad \hat{\mathbf{n}} \cdot \hat{\mathbf{z}} \geq 0 \\ & -\pi + \cos^{-1}(\hat{\mathbf{n}} \cdot \hat{\mathbf{z}}) & \text{if } \hat{\mathbf{n}} \cdot \hat{\mathbf{r}} < 0 \quad \& \quad \hat{\mathbf{n}} \cdot \hat{\mathbf{z}} < 0 \end{aligned}
\end{aligned} \tag{5}$$

Remember that this β corresponds to only ‘leading edges’ as non ‘leading-edge’ sub-surface never reach this step.

Find the velocity characteristic angle γ as:

$$\begin{aligned}
\gamma = & \begin{aligned} & \cos^{-1}(\hat{\mathbf{v}} \cdot \hat{\mathbf{r}}) & \text{if } \hat{\mathbf{v}} \cdot \hat{\mathbf{z}} \leq 0 \\ & -\cos^{-1}(\hat{\mathbf{v}} \cdot \hat{\mathbf{r}}) & \text{if } \hat{\mathbf{v}} \cdot \hat{\mathbf{z}} \geq 0 \end{aligned}
\end{aligned} \tag{6}$$

Find the surface characteristic angle ψ as:

$$\begin{aligned}
\psi = & \tan^{-1}((\hat{\mathbf{n}}_{r\theta} \cdot \hat{\mathbf{r}})/(\hat{\mathbf{n}}_{r\theta} \cdot \hat{\mathbf{r}})) \\
\text{where, } \hat{\mathbf{n}}_{r\theta} = & \frac{\hat{\mathbf{n}} - (\hat{\mathbf{n}} \cdot \hat{\mathbf{z}})\hat{\mathbf{z}}}{|\hat{\mathbf{n}} - (\hat{\mathbf{n}} \cdot \hat{\mathbf{z}})\hat{\mathbf{z}}|}
\end{aligned} \tag{7}$$

If $|\hat{\mathbf{n}} - (\hat{\mathbf{n}} \cdot \hat{\mathbf{z}})\hat{\mathbf{z}}| = 0$, set $\psi = 0$. In case both $\hat{\mathbf{v}}$ and $\hat{\mathbf{n}}$ align to $\hat{\mathbf{z}}$ ($\gamma = \pm\pi/2$ and $\psi = 0$), set $\hat{\mathbf{r}}$ in global x -direction.

Step 6: Calculate $\{\hat{\mathbf{g}} \cdot \hat{\mathbf{v}}, \hat{\mathbf{g}} \cdot \hat{\mathbf{n}}, \hat{\mathbf{n}} \cdot \hat{\mathbf{v}}\}$ using Eq 8 of the main text as:

$$\hat{\mathbf{g}} \cdot \hat{\mathbf{v}} = \sin \gamma, \quad \hat{\mathbf{g}} \cdot \hat{\mathbf{n}} = \cos \beta, \quad \hat{\mathbf{n}} \cdot \hat{\mathbf{v}} = \cos \psi \cos \gamma \sin \beta + \sin \gamma \cos \beta \quad [8]$$

and calculate f_1, f_2, f_3 using their dependencies on $\{\hat{\mathbf{g}} \cdot \hat{\mathbf{v}}, \hat{\mathbf{g}} \cdot \hat{\mathbf{n}}, \hat{\mathbf{n}} \cdot \hat{\mathbf{v}}\}$ from table S3 (or table S4). Note that these equations use following expressions of $\{\hat{\mathbf{n}}, \hat{\mathbf{v}}, \hat{\mathbf{g}}\}$ in $\{\hat{\mathbf{r}}, \hat{\boldsymbol{\theta}}, \hat{\mathbf{z}}\}$ coordinate frame:

$$\hat{\mathbf{g}} = -\hat{\mathbf{z}}, \quad \hat{\mathbf{v}} = \cos \gamma \hat{\mathbf{r}} - \sin \gamma \hat{\mathbf{z}}, \quad \hat{\mathbf{n}} = \sin \beta \cos \psi \hat{\mathbf{r}} + \sin \beta \sin \psi \hat{\boldsymbol{\theta}} - \cos \beta \hat{\mathbf{z}}. \quad [9]$$

Step 7: Calculate the values of $\{\alpha_r^{\text{gen}}, \alpha_\theta^{\text{gen}}, \alpha_z^{\text{gen}}\}$ using Eq 9 (of the main text) and table S3 (or table S4).

Step 8: Estimate the media specific scaling factor $\xi_n (= \rho_c g \hat{f}(\mu_{\text{int}}))$ using expected functional form of ξ_n from Table S1 and Fig S3 of the Supplementary Information if the media effective density (ρ_c), gravity magnitude (g), and media internal friction coefficient (μ_{int}) are known. Alternatively, obtain ξ_n from vertical plate intrusion experiments (intrusion of a thin flat plate of area ds at $\beta = 0$, $\psi = 0$, and $\gamma = \pi/2$) using the following formula:

$$\xi_n = \frac{F_{\text{vertical}}}{\alpha_z^{\text{gen}}(\beta = 0, \gamma = \pi/2, \psi = 0) \times ds \times |z|} \quad [10]$$

where, $|z|$ corresponds to the average depth of the plate from the free surface at which the force is measured.

Step 9: Calculate the sub-surface(s) specific α_n^{gen} and α_t^{gen} in the local coordinates (from the values of $\alpha_{r,\theta,z}^{\text{gen}}$ and $\hat{\mathbf{n}}$) and add them up using Eq 5 of the main text to get $\boldsymbol{\alpha}$.

Step 10: Calculate $\{\alpha_x, \alpha_y, \alpha_z\}$ by substituting triad $\{\hat{\mathbf{r}}, \hat{\boldsymbol{\theta}}, \hat{\mathbf{z}}\}$ from step 4.

Step 11: Calculate the net resistive force on the sub-surface by multiplying the triad $\{\alpha_x, \alpha_y, \alpha_z\}$ with sub-surface depth ($|z_i|$), and area (ds_i)

Step 12: Sum over all the sub-surfaces to find the net force and moment on the intruder.

Once the net resistive force on the intruder is known, one can use momentum balance equations to further model the intruder motion. Convergence studies are also done to determine the discretization of the intruder shape.

S8. DEM simulations

In this section, we discuss the details of DEM systems used for verifications studies. We use DEM based LIGGGHTS package for modeling grains. We use a 50/50 split of 3.0 mm and 3.4 mm diameter (d) grains in all the DEM simulations. More material properties are given in table S2. We use a simple shear simulation setup to determine the internal friction of the bulk of the granular volume. The setup consisted of a $100d \times 50d \times 90d$ granular bed in plane-strain condition and was sheared with rigid plates on the top and the bottom as shown in figure S6. For uniform shearing at constant pressure, a uniformly distributed constant force (F_{top}) was applied on the top plate whose motion was restricted to z -direction. An identical bottom plate was moved in positive x -direction to create the quasi-static simple shear condition.

Table S2. DEM material properties

Grain diameter (d)	50/50 split: 3 mm / 3.4 mm
Grain density (ρ_g)	2470 kg/m ³
Packing efficiency (ϕ)	~ 0.59
Contact model	Hookean contact model
Elastic modulus, E	7×10^6 N/m ²
Poisson's ratio, ν	0.45
Coefficient of restitution, e	0.88
Grain-grain friction, μ_{g-g}	0.05
Grain-surface friction, μ_{g-s}	0.4
Characteristic velocity	2

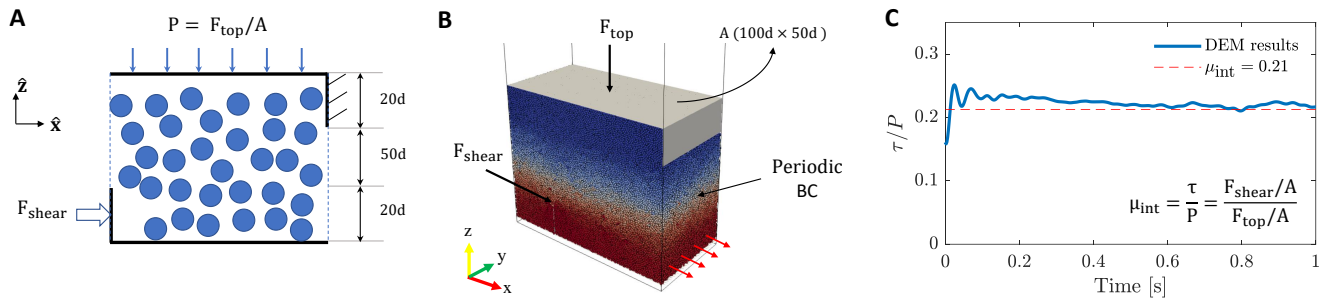


Fig. S6. Simple shear DEM setup: (A) 2D schematic and (B) 3D snapshot of the DEM simulation setup used for finding the internal friction coefficient of DEM particles used for verification studies. (C) Variation of the ratio of shear stress ($\tau = F_{shear}/A$) and pressure ($P = F_{top}/A$) as a function of time from DEM (solid blue line) and fitted estimate (red dotted line). Material properties are provided in table S2

145 **Radius of curvature corrections to DEM Bunny drill simulations:** As discussed in 3D-RFT premises, the RFT
 146 form assumes a scale separation by treating granular media as a continua. This assumption limits the performance of 3D-RFT
 147 when objects have sharp corners. While characterizing these effects would be a work for the future, we attempt to incorporate
 148 these effects at the most basic level in bunny drill simulations. This is important in the Bunny drill case especially because
 149 many features of the bunny shape have competing length scales to grain size in this DEM-based study. The grain size could
 150 not be reduced further in this study due to limitations on computational resources. Thus, we use a simple *Radius of curvature*
 151 (R_c) based identification of low- R_c regions of this intruder. We assume that any surface with a vertex with a radius of
 152 curvature lesser than 2 times the average grain radius will not experience any resistive force from the granular volumes. R_c
 153 was calculated using the discrete principle curvature formula from Hao Li's lecture notes (8). Figure S7 shows the radius of
 154 curvature estimation across the bunny shape used in this study.

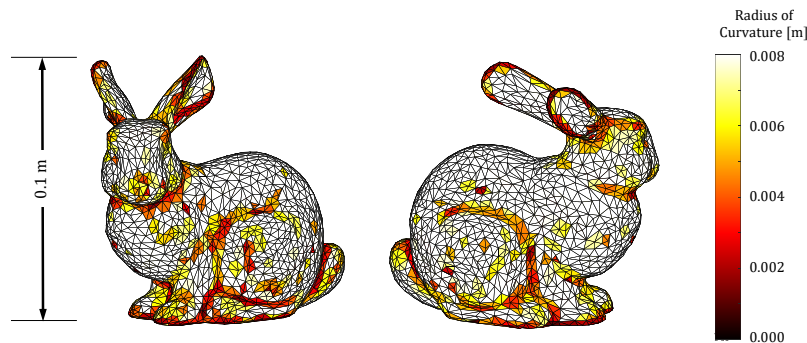


Fig. S7. Variation of radius of curvature (R_c) on Bunny shape: The colormap on the right shows the variations. R_c cut-off for active surfaces was set at 0.0048 m.

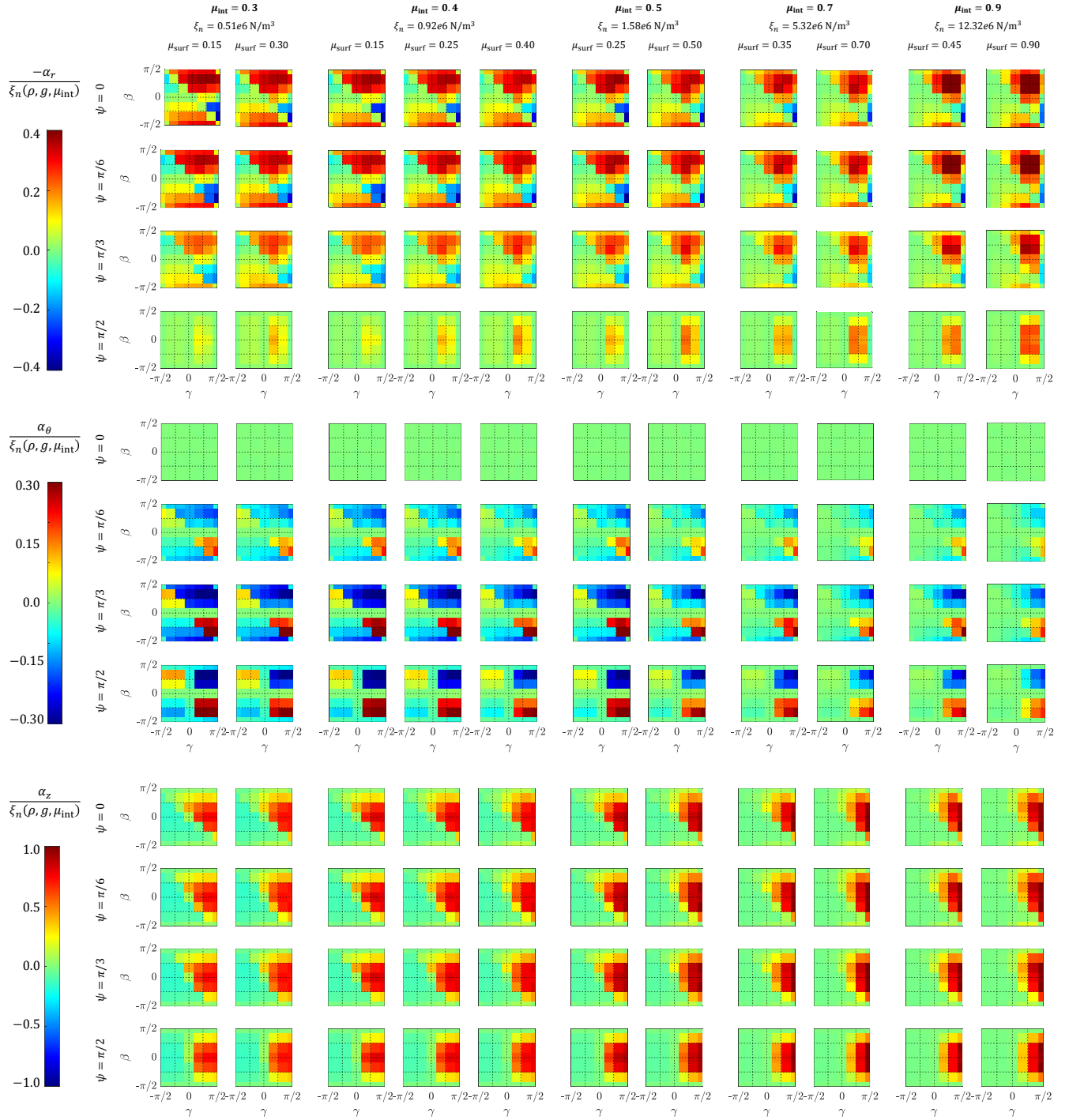


Fig. S8. 3D-RFT Raw data: Normalized $\alpha_{r,\theta,z}$ value for 3D-RFT reference data used for generation of 3D-RFT form. Corresponding values of μ_{int} , μ_{surf} , and ξ_n are written at the top of each column.

Table S3. f_1, f_2, f_3 3rd degree polynomial definitions

$$f_i = \sum_k c_i^k T_k = c_i^1 + c_i^2 p_1 + \dots + c_i^{19} p_1 p_2^2 + c_i^{20} p_1 p_2 p_3$$

$$[p_1 \equiv \hat{g} \cdot \hat{v} = \sin \gamma, \quad p_2 \equiv \hat{g} \cdot \hat{n} = \cos \beta, \quad p_3 \equiv \hat{n} \cdot \hat{v} = \cos \psi \cos \gamma \sin \beta + \sin \gamma \cos \beta]$$

k	T_k	c_1^k	c_2^k	c_3^k
1	1	0.00212	-0.06796	-0.02634
2	p_1	-0.02320	-0.10941	-0.03436
3	p_2	-0.20890	0.04725	0.45256
4	p_3	-0.43083	-0.06914	0.00835
5	p_1^2	-0.00259	-0.05835	0.02553
6	p_2^2	0.48872	-0.65880	-1.31290
7	p_3^2	-0.00415	-0.11985	-0.05532
8	$p_1 p_2$	0.07204	-0.25739	0.06790
9	$p_2 p_3$	-0.02750	-0.26834	-0.16404
10	$p_3 p_1$	-0.08772	0.02692	0.02287
11	p_1^3	0.01992	-0.00736	0.02927
12	p_2^3	-0.45961	0.63758	0.95406
13	p_3^3	0.40799	0.08997	-0.00131
14	$p_1 p_2^2$	-0.10107	0.21069	-0.11028
15	$p_2 p_1^2$	-0.06576	0.04748	0.01487
16	$p_2 p_3^2$	0.05664	0.20406	-0.02730
17	$p_3 p_2^2$	-0.09269	0.18519	0.10911
18	$p_3 p_1^2$	0.01892	0.04934	-0.04097
19	$p_1 p_3^2$	0.01033	0.13527	0.07881
20	$p_1 p_2 p_3$	0.15120	-0.33207	-0.27519

Table S4. $f_1, f_2,$ and f_3 function definitions with 4th degree polynomials

$$f_i = \sum_k c_i^k T_k = c_i^1 + c_i^2 p_1 + \dots + c_i^{19} p_1 p_3^2 + c_i^{35} p_1 p_2 p_3^2$$

$$[p_1 \equiv \hat{g} \cdot \hat{v} = \sin \gamma, \quad p_2 \equiv \hat{g} \cdot \hat{n} = \cos \beta, \quad p_3 \equiv \hat{n} \cdot \hat{v} = \cos \psi \cos \gamma \sin \beta + \sin \gamma \cos \beta]$$

k	T_k	c_1^k	c_2^k	c_3^k	k	T_k	c_1^k	c_2^k	c_3^k
1	1	0.00412	-0.06300	0.00892	2	p_1	-0.02136	-0.00336	-0.03143
3	p_2	-0.21785	-1.32520	-0.54392	4	p_3	-0.54991	0.00048	0.01939
5	p_1^2	-0.03285	-0.11116	-0.11861	6	p_2^2	0.87718	5.36790	2.03150
7	p_3^2	-0.00286	0.07983	-0.13326	8	$p_1 p_2$	-0.38369	0.08966	0.47638
9	$p_2 p_3$	0.48733	-0.11872	-0.35913	10	$p_3 p_1$	-0.16974	0.09029	0.13672
11	p_1^3	0.01923	-0.10024	0.01495	12	p_2^3	-1.82110	-7.53640	-2.44120
13	p_3^3	0.71170	-0.03393	-0.01711	14	$p_1 p_2^2$	1.03580	-0.48634	-1.14260
15	$p_2 p_1^2$	-0.06899	0.07279	0.20511	16	$p_2 p_3^2$	0.01924	0.15943	0.01142
17	$p_3 p_2^2$	-1.58070	-0.45871	0.52431	18	$p_3 p_1^2$	0.07461	0.10419	-0.03870
19	$p_1 p_3^2$	0.04814	-0.09860	0.10985	20	$p_1 p_2 p_3$	0.05565	-0.21270	-0.06686
21	p_1^4	0.02884	-0.02951	0.11721	22	p_2^4	1.10100	3.35300	0.90658
23	p_3^4	0.03094	-0.45255	0.03809	24	$p_1^3 p_2$	0.24807	0.07722	-0.25744
25	$p_1^3 p_3$	0.05269	-0.07405	-0.26752	26	$p_2^3 p_1$	-0.72304	0.32683	0.67218
27	$p_2^3 p_2$	1.15170	0.39561	-0.31197	28	$p_3^3 p_1$	0.20145	-0.13273	-0.11735
29	$p_3^3 p_2$	-0.09466	0.15479	0.06806	30	$p_1^2 p_2^2$	0.12995	0.08606	-0.12606
31	$p_1^2 p_3^2$	-0.06983	0.19846	0.18106	32	$p_2^2 p_3^2$	0.09628	0.29711	-0.02546
33	$p_1^2 p_2 p_3$	-0.57151	-0.07567	0.54032	34	$p_1 p_2^2 p_3$	-0.24520	-0.05941	-0.06226
35	$p_1 p_2 p_3^3$	0.03159	0.14051	-0.33556					

155 **References**

156 1. LK Treers, C Cao, HS Stuart, Granular resistive force theory implementation for three-dimensional trajectories. *IEEE*
157 *Robotics Autom. Lett.* **6**, 1887–1894 (2021).
158 2. L Huang, J Zhu, Y Yuan, Y Yin, A dynamic resistive force model for designing mobile robot in granular media. *IEEE*
159 *Robotics Autom. Lett.* **7**, 5357–5364 (2022).
160 3. H Askari, K Kamrin, Intrusion rheology in grains and other flowable materials. *Nat. materials* **15**, 1274–1279 (2016).
161 4. K Diaz, B Chong, S Tarr, E Erickson, DI Goldman, Water surface swimming dynamics in lightweight centipedes (2022).
162 5. CN Adkins, RH Liebeck, Design of optimum propellers. *J. Propuls. Power* **10**, 676–682 (1994).
163 6. J Gray, G Hancock, The propulsion of sea-urchin spermatozoa. *J. Exp. Biol.* **32**, 802–814 (1955).
164 7. W Kang, Y Feng, C Liu, R Blumenfeld, Archimedes’ law explains penetration of solids into granular media. *Nat.*
165 *communications* **9**, 1–9 (2018).

166 8. Hao Li , CSCI 599: Digital Geometry Processing, Differential operators on polygons (2015) <http://cs599.hao-li.com/>.